Proc. of SPIE, vol. 3261, pp. 193-207, January, 1998.

Computational Model of Image Formation Process in DIC Microscopy

Farhana Kagalwala[a] and Takeo Kanade[a]

[a]Carnegie Mellon University, 5000 Forbes Avenue, Pittsburgh, USA

ABSTRACT

A computational model of the image formation process has been developed for the Nomarski differential interference contrast (DIC) microscope. The DIC microscope images variations of the phase of the light wave transmitted through the specimen. In the study of biological phenomena, the DIC microscope is used to visualize live cells which are highly transparent in the visible spectra but distort the phase of the impinging light wave. Within the microscope, a birefringent prism splits the transmitted light wave into two laterally sheared wavefronts. An interference pattern is imaged when the wavefronts recombine.

The computational model we developed uses polarization ray-tracing techniques. Rays propagating through different microscope components and the specimen are traced. **A** specimen is represented by a 3-D grid of voxels, each containing a complex refractive index. At the image plane, a coherent superposition of the diffracted field due to each ray contributes to the image intensity. Partial coherence at the image plane is also simulated by wavefronts with different propagation directions. **By** computing the image intensity at different positions along the axial direction, we can obtain optically sectioned images.

In order to evaluate our model, we compared simulated images to the images taken under a real DIC microscope. We constructed test specimens of known shape and properties, using polystyrene beads in optical cement and an etched glass wafer. As the next step, we plan to use this computational model for the reverse problem, i.e. to reconstruct the 3D refractive index distribution of an imaged specimen.

Keywords: differential interference contrast, microscope, simulation, ray-tracing

1. INTRODUCTION

The Nomarski Differential Interference Contrast (DIC) microscope, the preferred method for obtaining phase information of biological specimens, images variations in the phase of the light wave transmitted through the observed specimen. Thus it can be used to imageobjects that distort predominantly the phase of the impinging light wave, and therefore are highly transparent in the visible spectra. Within the microscope, the impinging light wave is sheared along a transverse direction — perpendicular to the optical axis — into two wavefronts by a birefringent prism. The wavefronts propagate a differential distance apart through the specimen and their superposition causes an interference pattern to be detected at the image plane.

In the biological sciences, one use of the DIC microscope is to examine live specimens that might be adversely affected by the dyes used in fluorescence imaging. In addition, DIC optics can be used with high NA objectives and therefore has good optical sectioning characteristics. Optical sectioned images are a series of 2D images, each of which is taken with a different part of the object brought into focus.

The aim of the current work is to model the image formation process in DIC microscopy. Previous works dealing with DIC microscopy have formulated analytic models of the image formed by making various assumptions of the specimen and microscope parameters. We aim to use a more general technique, specifically a generalized ray-tracer, to calculate the intensity distribution at the image plane of the microscope. By using a general object model, the ray-tracer lifts assumptions on the object imposed by earlier works. In order to compare the accuracy of the simulation, images of real objects are compared to their simulated counterparts. The microscope model and the simulated images will be used in future work to reconstruct the actual shape and optical properties of the imaged specimen.

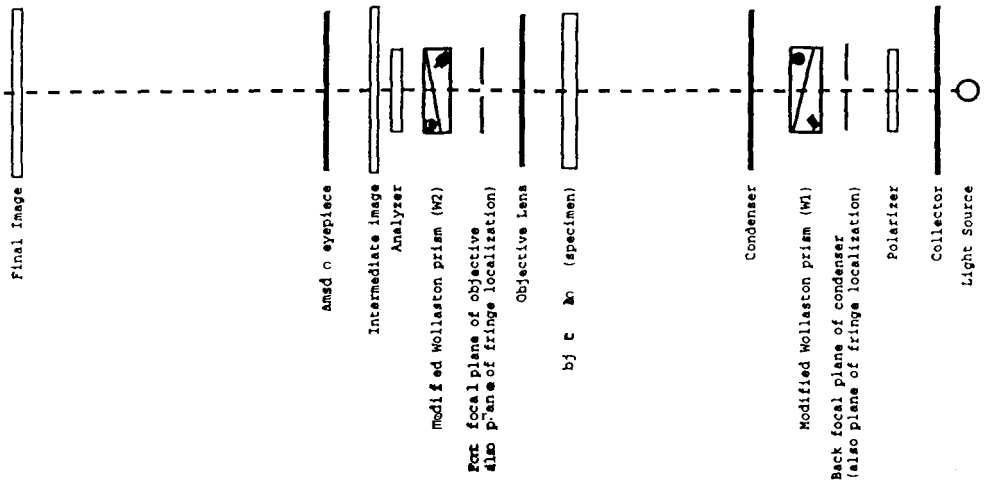

Figure 1. DIC Optical Components

2. DIC MICROSCOPE COMPONENTS

The Nomarski differential interference contrast (DIC) microscope can be viewed as a transmitted bright-field microscope with two crossed polarizers and two modified Wollaston (Nomarski) prisms[12] as shown in Fig. 1.

A light wave, emitted by the source at the right end of the figure, is focused by the collector. The light is usually filtered producing a beam with a narrow spectral composition. In our model, we assume a monochromatic wave of wavelength 640nm. The polarizer linearly polarizes the field in a direction 45° from the axis of the Wollaston prism (W1). The prism transversely shears the wavefront into two fields. Each field's amplitude is polarized orthogonal to the other. **Also,** the two fields propagate with a constant phase difference between them. The condenser focuses the beams into two transversely shifted waves which then travel through the specimen.

The objective back focal plane is coincident with the second modified Wollaston prism (W2). This prism is aligned such that it introduces a path difference exactly opposite to the one introduced by W1. If W2 is shifted transversely, in its plane, then some of the optical path length introduced by W1 is not canceled and a phase bias remains. This phase bias changes the interference pattern detected at the image plane. After passing through the analyzer, the two mutually coherent wavefronts can interfere causing an amplitude modulated light wave whose variations can then be detected.

3. COMPUTATIONAL MODEL

The computational model that we have developed consists of a polarized ray-tracer and an approximation of the diffraction effects. The model computes the light field at the image plane dictated by geometrical optics and convolves the field with a kernel representing the diffraction due to the objective aperture.

3.1. Representation of Light Rays

Using the principles of geometrical optics, a ray-tracer simulates the interaction of an impinging light wavefront with objects. Light rays are defined as the orthogonal trajectories to surfaces along which the phase values of the propagating field are constant. The surfaces of constant phase are generally called wavefronts. The orthogonal trajectories, or light rays, through an inhomogeneous medium can be represented by a space curve. Our specimen model consists of homogeneous objects only. In homogeneous media, light rays are vectors of the form,

$$\vec{\alpha}(t) = a' + \vec{k}t \qquad (1)$$

Other author information: (Send correspondence to F.K.)
F.K.: E-mail: farhana@cs.crnu.edu
T.K.: E-mail: kanadcQcs.ctnu.edu

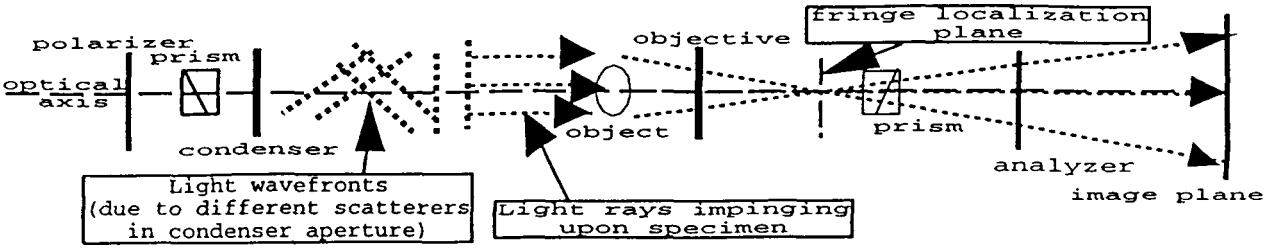

Figure 2. DIC microscope represented by our model

where $\vec{a}$ and $\vec{k}$ are constant vectors denoting the origin and the direction of the ray, respectively.

In our ray-tracer, we use vectors such as $\vec{\alpha}(t)$, to represent light rays. Therefore we approximate the wavefront by a tessellation of local planar regions. The distance between ray origins sampled on each wavefront determines the size of the local planar regions. In order to correctly interfere the two fields at the image plane, both the amplitude polarization and phase of the fields have to be calculated. Using a polarization ray model,[3] at each ray vector we store the local field amplitude polarization, propagation direction, and phase information. The origin of each ray, $\vec{a}$, determines where the ray was "born" and the distance along the ray—the value of t in Eq. 1—determines how far the ray has travelled from the origin in the propagation direction, $\vec{k}$. The local coordinate system at each ray is represented by the propagation vector $\vec{k}$ and two orthogonal vectors, $\vec{s}$ and $\vec{p}$, in the plane perpendicular to $\vec{k}$.

Any polarized field amplitude can be represented by two vectors orthogonal to the propagation directionsuch as $\vec{s}$ and $\vec{p}$ above— each of which is modulated by a complex scalar. The scalar coefficients of the polarized electric field, E_s and E_p are the components of Jones vectors. Therefore,

$$\vec{E} = \begin{bmatrix} E_s \\ E_p \end{bmatrix} = \begin{bmatrix} E_{0s}e^{i\phi_s} \\ E_{0p}e^{i\phi_p} \end{bmatrix} \tag{2}$$

represents the polarization state of a coherent wave.

In the current work, we have only simulated specimens that are composed of homogeneous objects. Therefore the vector ray model suffices to represent the light propagation through these objects. At the present time we are developing a more general model of light rays that can accurately represent the propagation of light through inhomogeneous media.

3.2. Representation of the Microscope

The microscope's optical components, which we model and show in Fig. 2, are represented as objects in a grid. The global coordinate system is aligned such that the z-axis is coincident with the optical axis and the x, y planes are transverse to the the optical axis. Each component is modelled as an ideal system.

We model the incoherence of scatterers at the condenser front focal plane. In our model, each scatterer results in two coherent planar wavefronts which are approximated by light rays with a particular direction impinging on the specimen. It should be noted that the contribution of light rays due to each individual scatterer is summed up coherently—field amplitudes are summed, whereas the contribution of light rays due to different scatterers is summed up incoherently—field intensities are summed.

3.2.1. Polarizer and Analyzer

The polarizer and analyzer, which are crossed, are modelled simply by Jones transfer matrices. Therefore the polarization of the field amplitude departing from the polarizer, $\bar{\vec{E}}$ is related to the incident field amplitude, $\vec{E}$ by

$$\begin{bmatrix} \bar{E}_s \\ \bar{E}_p \end{bmatrix} = L \begin{bmatrix} E_s \\ E_p \end{bmatrix} \tag{3}$$

where L is a matrix of the form,

$$L = \begin{bmatrix} (\cos\theta)^2 & \sin\theta\cos\theta \\ \sin\theta\cos\theta & (\sin\theta)^2 \end{bmatrix} \tag{4}$$

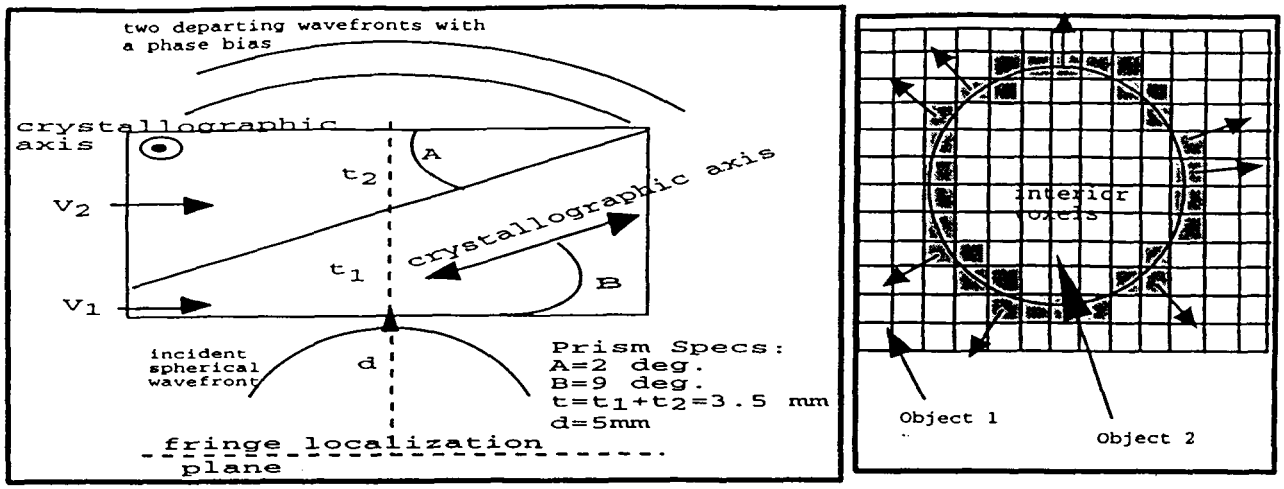

Figure 3. On Left: Modified Wollaston (Nomarski) prism model (made out of quartz) with one set of possible parameter values. On Right: Specimen model with some normals at object boundary voxels (shaded) shown.

3.2.2. Modified Wollaston (or Nomarski) Prism

The Modified Wollaston prism, otherwise known as the Nomarski prism (shown in Fig. 3), is a birefringent prism for which the plane where interference fringes are localized is located outside the prism.[4] The prism is built by joining two wedges, V_1 and V_2 in the figure, of a birefringent material—usually calcite or quartz. Each wedge is aligned such that the two crystallographic axes are orthogonal. Consider a spherical, linearly polarized, wave diverging from a point on the plane of fringe localization, and incident on one of the prism edges. Two splierical wavefronts with a constant relative phase depart from the opposite end of the prism. The relative phase bias between the wavefronts can be changed by shifting the prism transverse to the optical axis.

In DIC optics, one such prism is aligned so that its plane of fringe localization is coincident with the front focal plane of the condenser. Therefore each scatterer in this plane gives rise to a spherical wavefront. This wavefront is then sheared, by the prism, into two spherical wavefronts still diverging from the original point (refer to Fig. 3). The two spherical wavefronts are focused by the condenser into two coherent planar wavefronts with a constant phase bias between them. In our model, we only trace one ray from each point on the condenser front focal plane through the prism to determine the constant phase bias attributed to the corresponding planar wavefronts.

The direction of the planar wavefront, or the spatial frequency, is determined by the off-axial location of the corresponding scatterer in the condenser front focal plane. An identical prism is placed beyond the objective lens to introduce an exact opposite bias.

3.2.3. Objective Lens

The objective lens is modelled as an idealized lens, represented by a single refracting surface with negligible thickness. In reality, the objective lens is a multiple lens system that minimizes aberrations. Since the exact specifications are confidential, we assume an ideal lens modelled according to the available information. The numerical aperture, the focal length; the magnification and the working distances are reported by the manufacturer and are incorporated into our model. Diffraction of the wavefront by the lens aperture is calculated. The details are presented in Section 3.5.

3.3. Specimen Model

The specimen is represented by a 3-D grid of voxels, as shown in Fig. 3 and can contain multiple objects within it. A voxel can either be an interior, or a boundary voxel. A boundary voxel is defined as any voxel that intersects the bounding surface of an object. The boundary voxels contain a normal vector denoting tlie orientation of a plane passing through the center of that voxel. This vector is the normal at the point in tlie bounding surface wliicli is closest to the center of the voxel.

All voxels that are completely enclosed within the boundary of an object are called interior voxels and are labelled witli the refractive index value of the containing object. Within our paradigm, an object can exist within another

object. For example, a polystyrene bead can be embedded within optical cement. The optical cement medium and the bead are both considered objects, with the bead, shown as object 2 in the figure, contained completely within the optical cement, shown as object 1. In this case, any interior voxel enclosed by the bead would be labelled with the refractive index value of the bead. Whereas any voxel interior to the cement, but in the exterior of the bead would be labelled with the refractive index of the cement. Therefore, no exterior voxels can exist within this framework.

This specimen model assumes that each object has a homogeneous refractive index distribution. At present we are incorporating a more general specimen model that represents inhomogeneous objects as well.

3.4. Interaction of Light Rays and Matter

At each object boundary, the incident ray gives rise to two new rays, a reflected ray and a refracted one. The directions of the two new rays are computed using Snell's propagation laws. In addition, Fresnel's reflection/transmission coefficients are used to calculate the appropriate amplitude polarization and phase components for the new rays.

In the plane of incidence, $\theta_i = \theta_r$ and $n_i \sin\theta_i = n_t \sin\theta_t$, where θ_i is the angle between the surface normal and the incident ray, θ_r is the angle subtended by the reflected ray and θ_t is the angle subtended by the transmitted ray. The former equation can be written in terms of the incident and transmitted rays' propagation directions, $\vec{k}_i$ and k_t respectively, as $n_i \left(\vec{k}_i \times \vec{u}_n\right) = n_t \left(\vec{k}_t \times \vec{u}_n\right)$, where $\vec{u}_n$ is the surface normal at the intersection point. $\vec{u}_n$ corresponds to the surface normal stored at each boundary voxel.

The Fresnel equations determine the field components at the intersection of two linear, isotropic, homogeneous media.' Each field polarization component has to be transformed from the ray's local coordinate system into two components perpendicular and parallel to the incident plane. The reflected and transmitted fields, perpendicular and parallel to the incident plane, are weighted by the appropriate reflection and transmission coefficients. The equations for the amplitude coefficients applied to the reflected and transmitted field perpendicular to the incident plane are, respectively,

$$r_\perp = \frac{n_i \cos\theta_i - n_t \cos\theta_t}{n_i \cos\theta_i + n_t \cos\theta_t} \tag{5}$$

$$t_\perp = \frac{2 n_i \cos\theta_i}{n_i \cos\theta_i + n_t \cos\theta_t} \tag{6}$$

While the amplitude coefficients applied to the field parallel to the incident plane are

$$r_\parallel = \frac{n_t \cos\theta_i - n_i \cos\theta_t}{n_i \cos\theta_t + n_t \cos\theta_i} \tag{7}$$

$$t_\parallel = \frac{2 n_i \cos\theta_i}{n_i \cos\theta_t + n_t \cos\theta_i} \tag{8}$$

The transmitted field components do not undergo any phase shifts if the incident angle is less than the critical angle under which total internal reflection occurs. On the other hand, the reflected field components will change phase under certain circumstances.

Absorption by a material is modelled using the complex refractive index, $n = n_r + j n_i$ where $(n_i \neq 0)$. If a disturbance propagates in the X-direction in a material with the aforementioned refractive index,

$$E = \left[E_0 \exp^{-(\omega n_i x)/c}\right] \exp^{i\omega(t - n_r x/c)}, \tag{9}$$

then its amplitude attenuation is represented by the first bracketed quantity. The complex part of the refractive index determines the material's absorption. As the light ray travels a distance d through any object ($n_r \geq 1.0$) the path length, $\delta = d(n_r - 1)$ and the phase $\phi = 2\pi\delta/\lambda$ is calculated.

3.5. Image Formation

Light rays which travel through the prism, with fringe localization plane at the back focal plane of the objective, intersect the image plane. The image plane, centered around and perpendicular to the optical axis, is modelled as a two-dimensional hash table with bins representing the discrete pixels of a CCD array.

As each ray intersects a bin, its phase and polarization is recorded at that location. The orientation of the energy field with respect to the image plane determines energy contribution by that ray. The scalar product of the ray propagation direction vector with the image plane normal ($\cos\theta_j$ in Eq. 10) modulates the amplitude of the energy contribution by that particular ray. The phase of the ray is recorded and is used to calculate the interference between the contributions of different rays. The complex amplitudes of all the rays (due to a particular scatterer in the condenser front focal plane) are added together and the squared magnitude (intensity) of the resulting sum is recorded at that particular pixel. The intensity contributions of rays due to different scatterers are then added together to calculate the total intensity value at that image pixel. Therefore, ignoring diffraction effects for the moment, the resulting intensity at a pixel (m,n) which contains N_k rays from the k^{th} scatterer in the condenser front focal plane can be represented by

$$I_{m,n} = \sum_{k=1}^{K} \left| \sum_{j=1}^{N_k} \cos\theta_j \left[E_j^s \exp^{i\phi_j^s} + E_j^p \exp^{i\phi_j^p} \right] \right|^2 \tag{10}$$

$$= \sum_{k=1}^{K} \left| \sum_{j=1}^{N_k} \cos\theta_j \left[\left(E_j^s \cos\phi_j^s + E_j^p \cos\phi_j^p \right) + i \left(E_j^s \sin\phi_j^s + E_j^p \sin\phi_j^p \right) \right] \right|^2 \tag{11}$$

where E_j^s and E_j^p are the amplitudecomponents, and ϕ_j^s and ϕ_j^p are the respective phases represented by the j^{th} ray.

In the limit that the wavelength approaches zero, the intensity distribution at the image plane as described above would be accurate. In reality, with a finite wavelength and a finite extent of the objective's aperture, diffraction by the aperture has to be incorporated into the model. Consequently, in our model we treat the field as a wave beyond the objective lens aperture. The above developments were modified so that each ray contributes energy to more than one pixel bin. A simple two-dimensional Fraunhofer diffraction pattern cannot be used to accurately describe the image. The three-dimensional light distribution near the focal point has to be calculated.

In order to compute the diffracted field at the image plane, we assume points in the specimen give rise to diverging spherical wavefronts (Huygens wavelets). The spherical wavefronts are transformed by the objective lens into wavefronts of opposite curvature, which then converge to their respective geometrical image points. We also assume that all the converging spherical wavefronts are diffracted by the objective aperture, and that these diffracted waves then linearly superpose in the image plane. At each point in the image plane, there is a contribution from all the converging spherical wavefronts. For each ray leaving the object, the location of the image plane can be determined by the lens law, $1/s_i + 1/s_o = 1/f_l$, where s_i is the distance from the center of the lens to the image plane, s_o is the distance to the object plane and f_l is the focal length of the lens. The geometrical image point is computed by intersecting the ray with the image plane. An ideal spherical wavefront leaving the objective lens would converge to the geometrical image point. The diffracted wavefront contributes to all pixels in a neighborhood of the geometrical image point. At each point in the image we compute the amplitude contribution of each wavefront due to each traced ray, using an approximation[6] of the following integral

$$U(\vec{x}_i) = \frac{-i}{2\lambda} \int\int_a \frac{|u(A)| \exp[-ik(r-s)]}{s} \times [\cos(\vec{n},\vec{r}) - \cos(\vec{n},\vec{s})]\, dS \tag{12}$$

where $\vec{x}_i$ is the image point, A is the entire aperture surface, $\vec{r}$ is the vector from the aperture point to the point of convergence of the spherical wavefront, $\vec{s}$ is the vector from the aperture point to $\vec{x}_i$, $\vec{n}$ is the normal at the aperture point and $|u(a)|$ is the magnitude of the amplitude of the spherical wavefront on the aperture surface A.

Table 1. Specifications of the objective lens as reported by Zeiss, Inc.

Parameter	Value
Numerical Aperture	**1.3**
Magnification	100X
Focal Length	1.63 mm
Working Distance	0.06 mm
Pupil Diameter	4.2mm
Resolution	**26** angstroms

4. IMPLEMENTATION DETAILS

A recursive ray-tracing algorithm, calculating the interaction of rays at multiple surface boundaries, was used to build the DIC microscope model. **For** a specific plane wave, rays are sampled along the planar wavefront past the condenser. Each initial ray is a root node of a ray tree. Two new rays, the two children of the node representing the incident ray, emerge at each object boundary. In this manner, ray trees are built for each sampled ray. We use the voxel-traversal algorithm developed by Amanatides and Woo to efficiently propagate rays through the uniform voxel grid.'

Images at multiple object planes are calculated using the resulting trees from just one ray-casting.

The sampling rates for the initial planar wavefronts are determined **by** the frequencies present at the output image plane. These frequencies are a result of the diffraction phenomena. It has been shown[8] that the number of total samples in the x (N_x) and the y (N_y) directions needed to accurately sample the diffraction effects is

$$N_x = \frac{L_{ix}\,(L_{ix} + L_{ox})}{\lambda z} \tag{13}$$

$$N_y = \frac{L_{iy}\,(L_{iy} + L_{oy})}{\lambda z}, \tag{14}$$

where L_{ix} and L_{iy} are the extents of the image, and L_{ox} and L_{oy} are the extents of the object.

At runtime, a data file is used to input the general optics setup of the microscope, including objective and condenser lens parameters and prism specifications. The specimen objects can be specified in the data file or via a Motif interface dialog box. The transmission and reflection properties of objects are also input at runtime.

5. RESULTS

In order to access the accuracy of our simulation, we created two different test samples.

5.1. Bead Test Samples

We created test specimens consisting of polystyrene beads of **4** micron and 10 micron diameters embedded in optical cement. Beads were embedded in a thin layer of optical adhesive with refractive indices ranging from 1.56 to 1.52. The refractive index of the beads ranged from 1.58 to 1.59. Different optical cements were used to study any image artifacts caused by large abrupt refractive index variations between the objects. Creating the sample required spin-casting a solution containing the beads across a microscope slide. Then adding a drop of optical cement onto the slide and treating the sample with UV light to harden it.

Using a Zeiss Inverted Multi-Mode microscope, we obtained several optically sectioned data sets of the specimen. Some of the images are shown in Fig. 4. The objective lens, a Zeiss Plan Neofluor, specifications are given in Table 1.

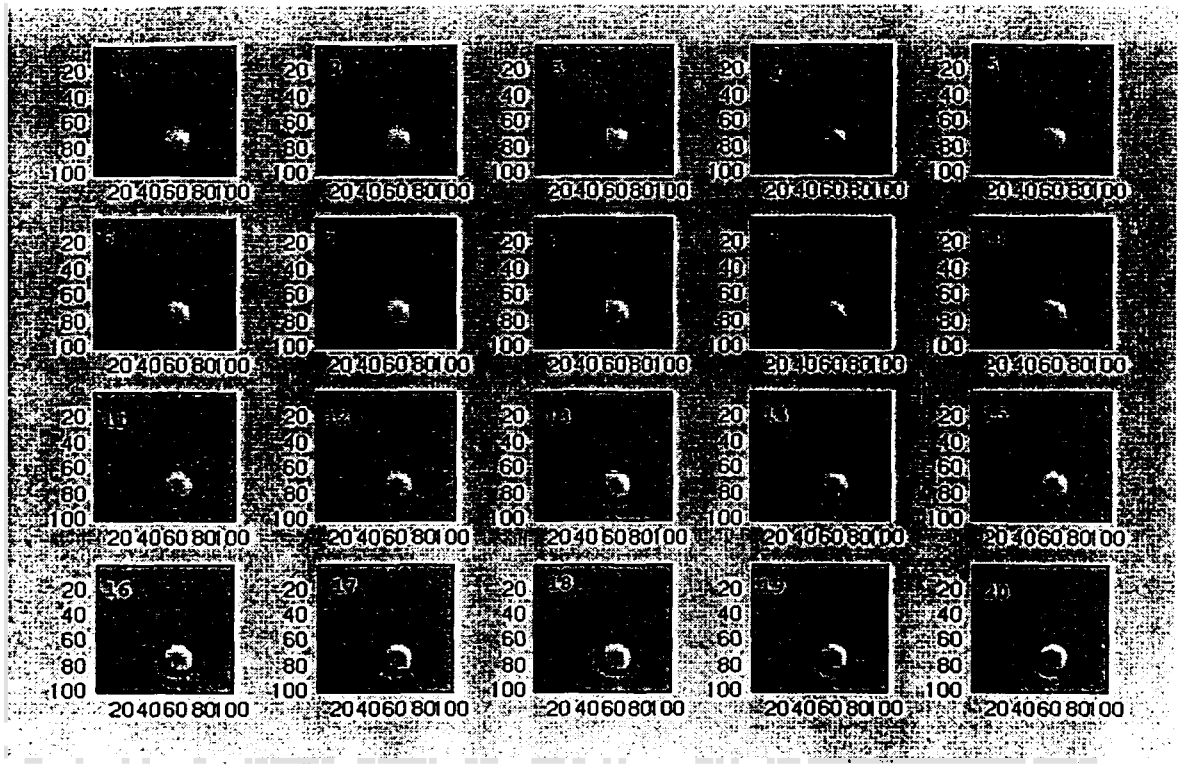

Figure 4. Real, through focus images of 10 micron diameter polystyrene bead. Each slice is .2 microns apart. Each image beginning from the first is increasingly more focused.

5.2. Etched Glass Test Samples

An etched glass sample was created using photo-lithography and ion-milling. Using this method of fabrication, the etched distance can be determined within a tolerance of 100 angstroms. The surface of a Corning glass wafer, such as the one we used, is assured to be optically flat and the optical properties (index of refraction, transmission, and absorption) are well-documented. The index of refraction for glass is **1.523** (defined in light of 589.3 nm) and the absorption is 7% of light intensity (for light of wavelength 640nm) per 1mm of glass.

Our sample, diagrammed in Fig. 6, is .5mm thick and 1 inch in diameter. Each etched square in this wafer contains several etched rectangles. Each rectangle has a depth of .3 microns. The boundaries of the rounded rectangular depression are sloped.

This wafer was imaged first with a glass-air interface at the rectangular depression, which proved to have too large a refractive-index disparity to acquire reliable DIC images. After some experimentation, the wafer was imaged with water' filling the rectangular cavity. DIC images of a section of the wafer are shown in Fig. 7 and Fig. 8.

5.3. Discussion of Results

The qualitative comparisons of the real, in-focus image data with the simulated, in-focus image data show that the general properties of the intensity distribution across the images are very similar. The general shadow-cast effect of DIC images is captured by the simulated images. In addition changing microscope parameters results in the appropriate changes in the simulated images. For example, images with different shear directions are shown in Fig. 10. **Also,** in the simulated images, changes in shear amount results in larger or smaller shadows when appropriate, but since this cannot be compared to real data (prism shear amount cannot be changed on the real microscope) we omit pictures.

*The refractive index of water is 1.3330 for wavelength of 587.6 nm

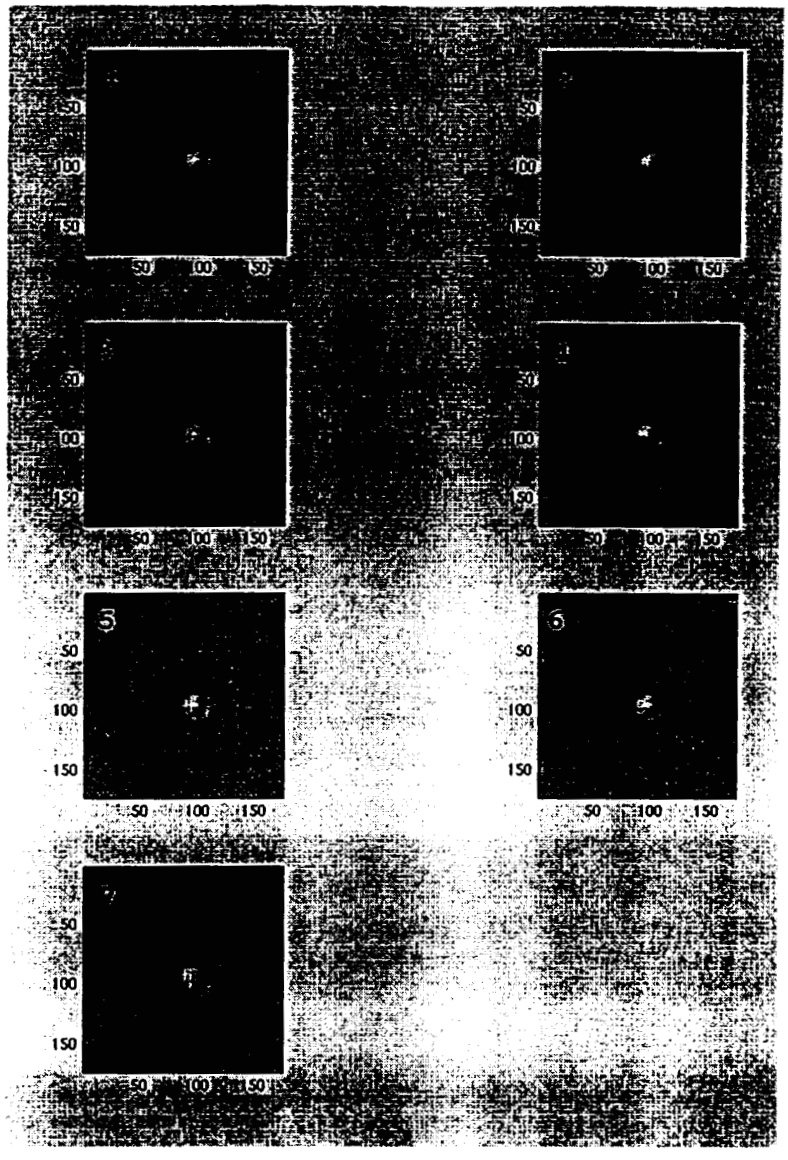

Figure 5. Simulated images of a 4 micron diameter sphere with refractive index 1.59 embedded in cement of refractive index 1.56. The topleftmost image is in focus, while each successive image is slightly more defocus-ed.

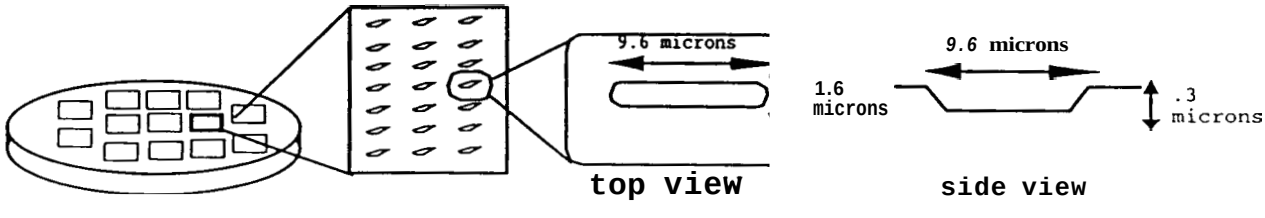

Figure 6. Schematic of the fabricated test sample.

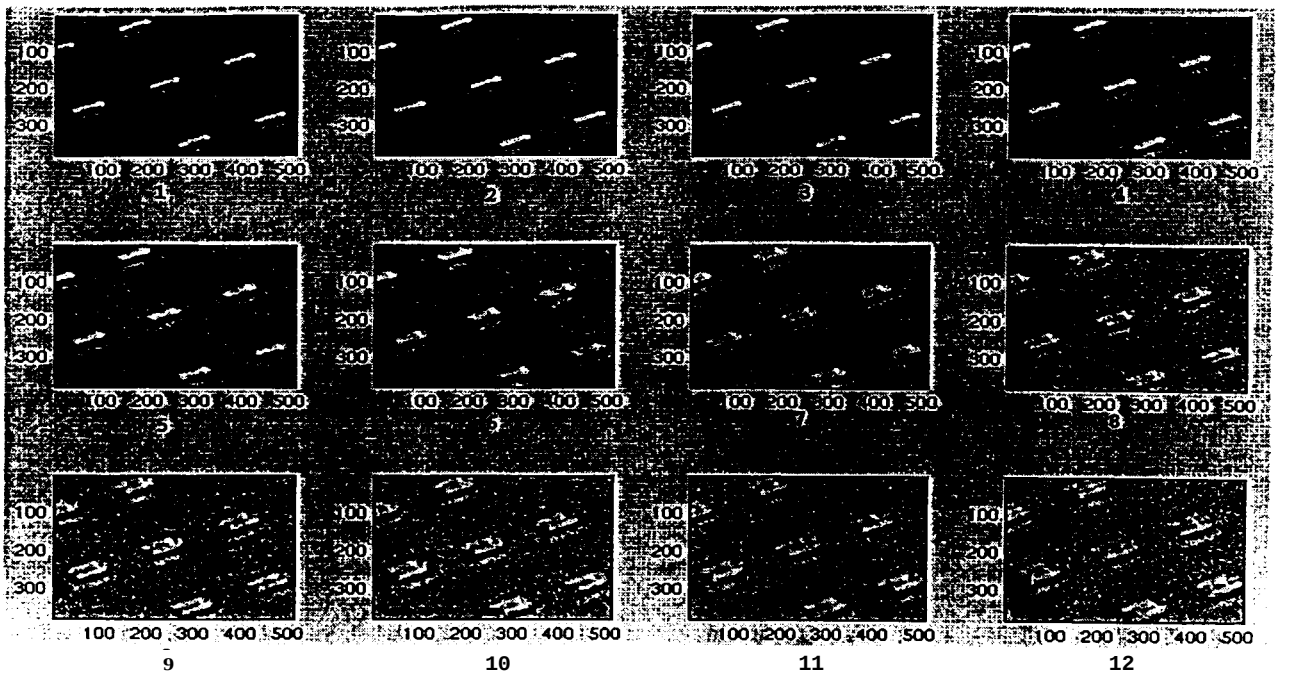

Figure 7. Through focus images of section of real wafer. **Each** slice is taken at a .2 micron spacing. The first image is in focus and each consecutive image is increasingly out of focus.

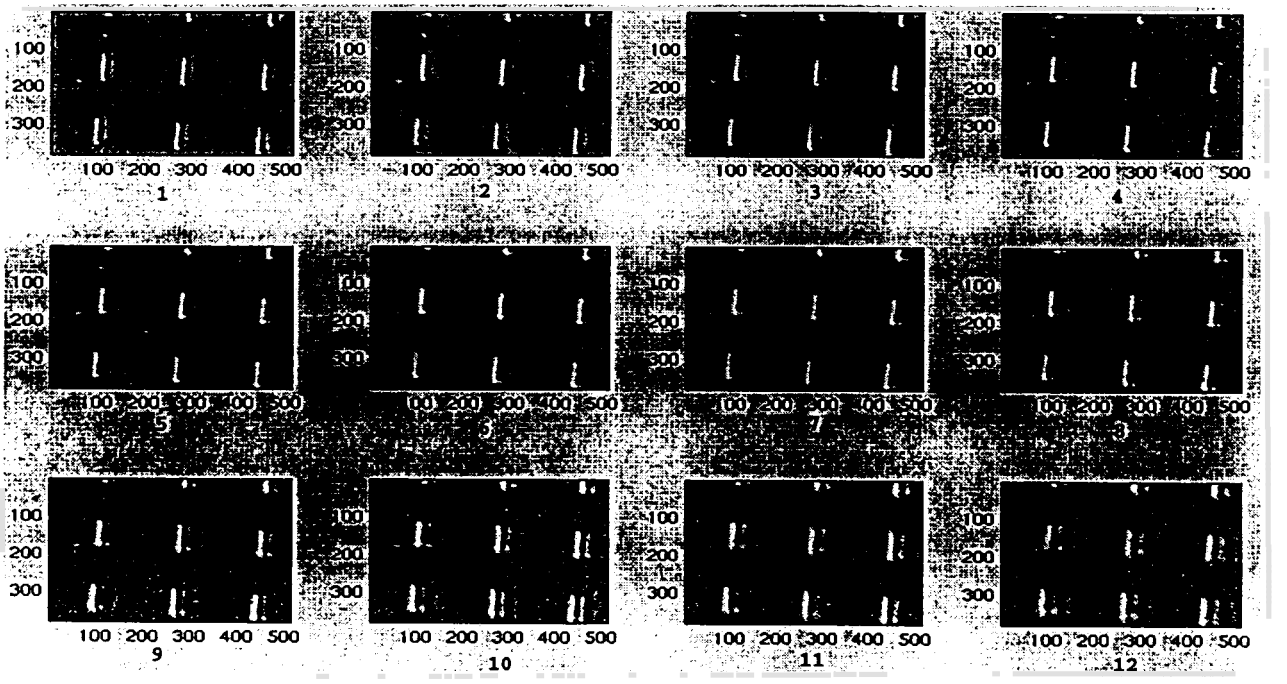

Figure *8.* Through focus images of section of real wafer. Each slice is taken at a .2 micron spacing. The object has been rotated so that the images are taken at a different shear direction from the previous images. As above, the first image is in focus and the consecutive ones are increasingly out of focus.

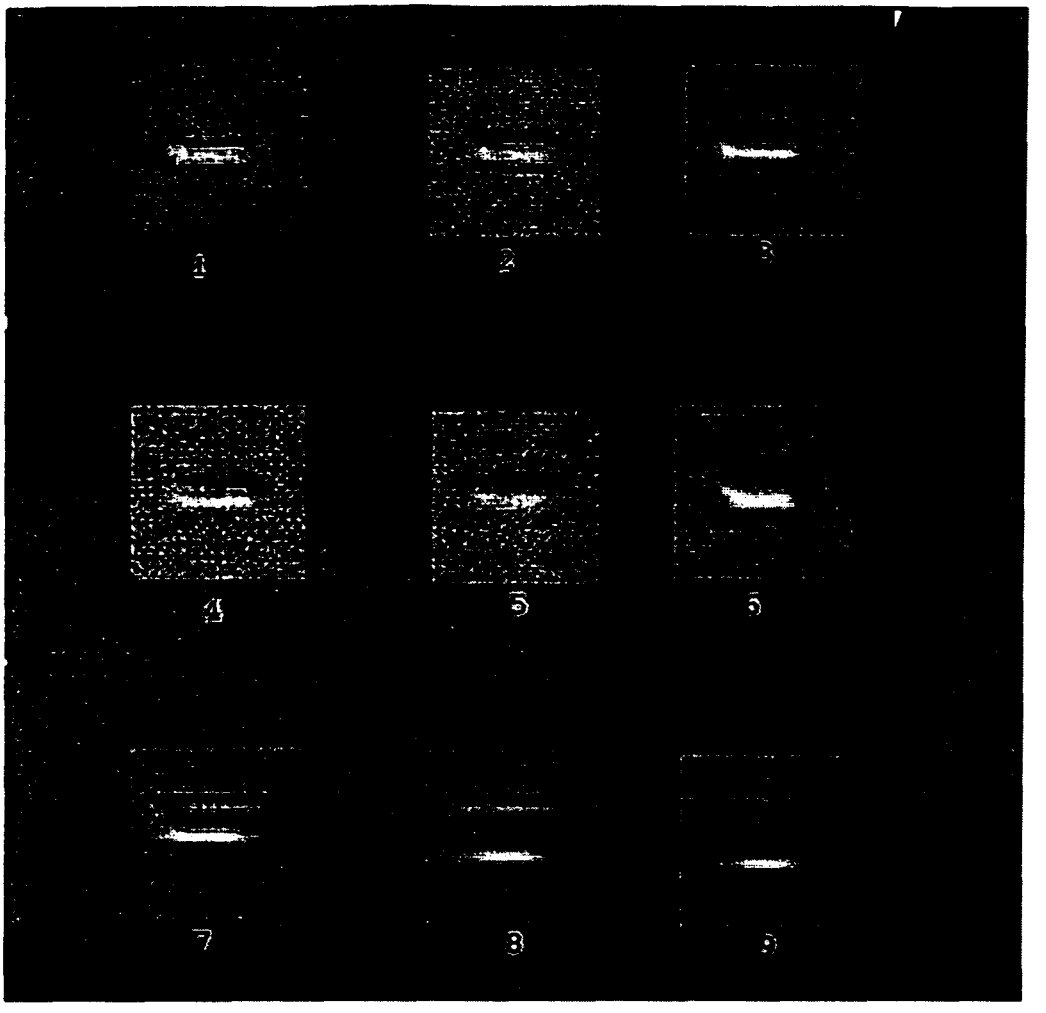

Figure 9. Simulated images of one of the rectangles in the etched wafer. The topleftmost image is the in-focus image with each successor image (to the right and from top to bottom) increasingly out of focus.

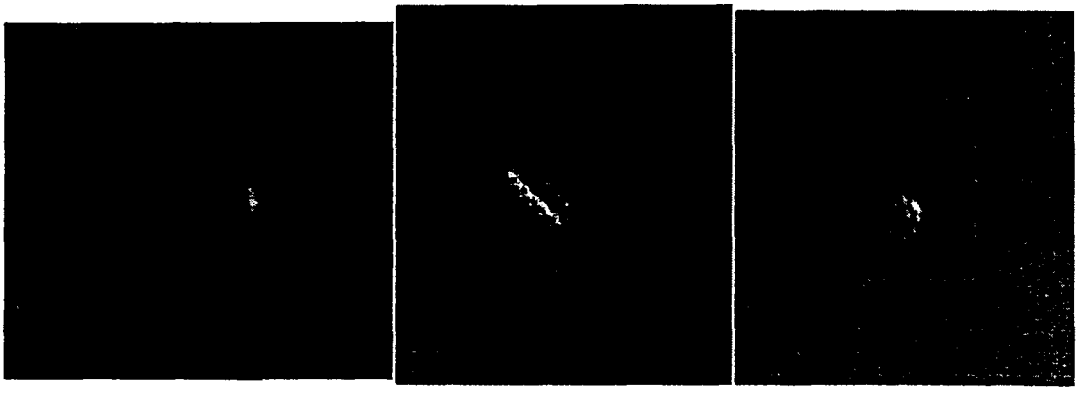

Figure 10. Simulated images of both samples with different shear directions.

The largest deviations from real data appear in the out-of-focus simulations. Although, in these images, the general blurring effects are present, there appear to be significant differences between the simulated and real images. These effects could be attributed to our simple diffraction model, i.e. we ignore polarization effects and any optical non-linearities, and assume that off-axial points have the same amplitude point-spread function as axial points.

6. CONCLUDING REMARKS

In this current work, we have demonstrated that the image-formation process in DIC microscopy can be simulated to some degree of accuracy using our computational model. Though real out-of-focus images have significant deviations from their simulated counterparts, the general shared properties are of the largest importance to us. Currently we are working on a more generalized ray and specimen model that will incorporate propagation through heterogeneous—but still isotropic—media and more complete diffraction calculations. Our future goals include developing an algorithm that reconstructs the optical properties and shape of the specimen using this computational model.

ACKNOWLEDGMENTS

The authors would like to thank the members of the Center for Light Microscope Imaging and Biology at Carnegie Mellon University. Specifically, Professor Frederick Lanni for his invaluable advice and Mr. Greg LaRocca for his help with obtaining images. In addition, the authors would like to thank **Dr.** Suresh Santharam for his help in creating the wafer sample. This work was made possible by the NSF Training Fellowship **for** Light Microscope Imaging awarded to the first author.

REFERENCES

1. G. D. R.D. Allen and G. Nomarski, "The zeiss-nomarski differential interference equipment for transmitted light microscopy," *Z.wiss. Mikrosk.* **69,** pp. 193–221, 1969.
2. W. Galbraith and G.David, "An aid to understanding differential contrast microscopy: computer simulation," ***Journal of Microscopy*** **108:2**, pp. 147–76, 1976.
3. R. Chipman, "Mechanics of polarization ray tracing," ***Optical Eng.*** **34:6,** pp. 1636–45, 1995.
4. M. Pluta, ***Advanced Light Microscopy, Volumes 1 and 2.***, Elsevier Science, New York, 1988.
5. M. Born and E. Wolf, ***Principles of Optics, Sixth Edition,*** Pergamon Press, Oxford, 1980.
6. S. Gibson and F. Lanni, "Diffraction by a circular aperture as a model for three-dimensional optical microscopy," *J.Opt.Soc.Am.,A* **6:9**, p. 1357:67, 1989.
7. J. Amanatides and A. Woo, "A fast voxel traversal algorithm for ray-tracing," ***Proceedings of Eurographics*** **1,** pp. 3–11, 1987.
8. J. Goodman, ***Introduction to Fourier Optics,*** McGraw Hill, New York, 1996.